IEEE Access
Multidisciplinary | Rapid Review | Open Access Journal

Received January 19, 2018, accepted March 11, 2018, date of publication March 26, 2018, date of current version May 16, 2018.

Digital Object Identifier 10.1109/ACCESS.2018.2817359

Multicarrier SAR Image Reconstruction Using Integrated MUSIC-LSE Algorithm

MOHAMMED D. BUHARI[1], (Graduate Student Member, IEEE), GUI YUN TIAN[1,2], (Senior Member, IEEE), RAJESH TIWARI[1], (Member, IEEE), AND ALI H. MUQAIBEL[3], (Senior Member, IEEE)

[1]School of Engineering, Newcastle University, Newcastle upon Tyne NE1 7RU, U.K.
[2]School of Automation Engineering, University of Electronic Science and Technology of China, Chengdu 611731, China
[3]King Fahd University of Petroleum and Minerals, Dhahran 31261, Saudi Arabia

Corresponding author: Gui Yun Tian (g.y.tian@uestc.edu.cn)

This work was supported in part by the National Natural Science Foundation of China under Grant 61527803, in part by the Novel Sensing Networks for Intelligent Monitoring (NEWTON) under Grant EP/J012343/1, and in part by the Petroleum Trust Development Fund Nigeria.

ABSTRACT In synthetic aperture radar (SAR) applications, high-resolution images and effective estimation processes are vital for the reconstruction of any targets. This can be achieved by using multicarrier waveforms such as orthogonal frequency division multiplexing (OFDM) with the help of appropriate signal processing algorithms. However, the quality of the reconstructed image degrades in low signal-to-noise ratio (SNR) environments during SAR data acquisition. In this paper, an integrated multiple signal classification (MUSIC) assisted least square estimation (LSE) algorithm (MUSIC-LSE) is proposed to enhance the quality of the reconstructed SAR image in a low-SNR environment. Simulation results measured and evaluated the quality of the reconstructed image using three performance indicators of root-mean-square-error, main lobe width and cumulative side lobe levels. These indicators are also used to investigate the effect of OFDM subcarrier selection on the reconstructed image for a different number of subcarriers. Experimental validation of the approach is carried out using two steel pipes to image and detect the curvature of the steel pipes. The results show that the proposed MUSIC-LSE approach produces better-reconstructed images compared with the existing linear frequency modulated (LFM) chirp and OFDM-LSE approaches in low-SNR (-10 dB) environments and enables the radar to distinguish and detect the curvature of the pipes even below the radar range and cross-range resolution.

INDEX TERMS Image reconstruction, LSE, MUSIC, orthogonal frequency division multiplexing (OFDM), signal-to-noise ratio (SNR), synthetic aperture radar (SAR).

I. INTRODUCTION

In remote sensing based applications, synthetic aperture radar (SAR) is one of the techniques used to provide high-resolution radar images of the terrestrial surface of the Earth. This is achieved by mounting the radar sensor on a moving platform such as aircraft, unmanned aerial vehicle (UAV) or ground moving object. The main advantages of SAR over optical imaging is that it is independent of weather conditions, providing consistent images of an environment irrespective of whether it is day or night [1]. As development and progression of the Earth observatory systems evolve for military and civilian applications, accurate and high-resolution radar images are required. The signal processing of different SAR systems and their image reconstruction algorithms illustrate different strengths and limitations in handling radar cross section (RCS) scintillations and combating target fading [2]. In terms of the SAR signal waveform, linear frequency modulated (LFM) chirp is a well-studied waveform and uses the classical approach of range-Doppler (RD) performed in the frequency domain to process the structure of the collected signal [3]. In [4], an improved RD imaging algorithm was proposed for a frequency modulated continuous waveform (FMCW) SAR to minimize the range and cross-range ambiguity associated with FMCW waveforms. Whilst in [5], LFM SAR was used as an alternative to time-domain methods by controlling the phase approximation errors of the reconstructed target. The concept of multicarrier orthogonal frequency division multiplexing (OFDM) was first introduced in SAR by Garmatyuk due to the desire to enhance image quality and to fully utilize the radar system bandwidth,

which directly controls the resolution in range [6]. It also provides a SAR signal design for non-LFM waveforms to achieve adaptability with a low probability of intercept and to exploit the frequency diversity of target returns. In [7], an adaptive OFDM SAR was proposed for a single point target and the method was validated via numerical simulation. Reference [8] proposed a cyclic prefix (CP) based OFDM SAR imaging technique for inter-range cell interference (IRCI) and achieved, in the ideal case scenario, zero side lobes for range reconstruction in a noise-free environment. They also showed that the OFDM subcarriers must be at least twice the number of range cells in a given SAR swath.

In addition to SAR signal waveforms, different signal processing algorithms have been applied for SAR image reconstruction to provide high-resolution images such as wavenumber domain ($\omega - \kappa$), back projection, range-doppler and beam formation algorithms [9], [10]. Most of these classical SAR algorithms assume that the targets are made up of a set of isotropic scatterers which are not suitable for man-made targets [11]. In [[12], an improved phase retrieval (PR) algorithm was proposed to improve radar image quality by adding a filter to the conventional PR algorithm. This reduced the influence of background noise on the reconstructed targets at a signal-to-noise ratio (SNR) of 20 dB. Whilst in [13], sparsity-driven SAR imaging for a ground target through the combination of time-frequency analysis and parametric Bayesian learning were studied. In [14], a novel high-resolution range profile (HRRP) using a sparse frequency-stepped chirp signal (FSCS) was proposed. The approach showed that even with an incomplete number of subpulses of FSCS, the HRRP can still reconstruct the target successfully. Recent studies in [15] and [16], proposed least square estimation (LSE) to estimate the OFDM SAR phase history (Doppler shift) and match filtered it with a reference function to reconstruct the target. This improves the quality of the reconstructed image as LSE gives a better estimate of the target position.

Despite the aforementioned developments in SAR, the quality of the reconstructed image degrades in a dense environment with low SNR (-10 dB) which makes it difficult for the radar to distinguish multiple targets within the reconstructed image. This is because, for the case of multicarrier OFDM, as the number of subcarriers increases (which leads to a high rate of data acquisition), signal fading due to multipath and cross interference occurs and this is a serious challenge at low SNR, resulting in performance degradation [17]. There is also a need to investigate the behaviour of the reconstructed OFDM SAR image for a different number of subcarriers to determine the optimal number of subcarriers to use for a given OFDM SAR system. Attempts were made to solve these problems by estimating the received signal direction of arrival (DoA) using algorithms such as multiple signal classification (MUSIC), root-MUSIC and estimation of signal parameters via rotational invariance technique (ESPRIT) [18], [19]. Although both ESPRIT and root-MUSIC give a better performance compared to MUSIC, MUSIC is utilised in this study for the following reasons. In relation to ESPRIT, ESPRIT requires twice as many sensors as MUSIC and considering that the approach will be applied in SAR image reconstruction; it makes the practical implementation of the system more expensive compared to MUSIC. With regards to root-MUSIC, the latter is only applicable to a uniform spaced linear array and hence cannot be used with a non-uniformly spaced array system [20]. In radar applications, MUSIC algorithms have been used in works including clutter cancellation in passive radar [21] and range-azimuth target location in FMCW radar systems [22]. Reference [23] proposed an improved compressive sensing (CS) approach for high-resolution radar imaging to overcome the high degree of noise and clutter associated with the radar image in low SNR systems. These authors combined coherent projections and weighing using CS optimisation for Inverse SAR image formation for low SNR systems ranging from 2 to 8 dB. In [24], an angular super-resolution scanning radar was proposed based on virtual array mapping. The virtual uniform linear array (ULA) was estimated and the target distributions recovered using the MUSIC algorithm. The method was validated via numerical simulation. However, the authors assumed a noiseless model that cannot resolve or give high-resolution images below an SNR of 10 dB. Recently, [25] combined a range-cell-focusing algorithm with the MUSIC algorithm for SAR target imaging. MUSIC was applied to the SAR raw data in a time domain after which range-cell focusing was applied. This approach improves the quality of the image at a low SNR of up to 5 dB. In [26], we proposed an integrated MUSIC assisted LSE algorithm (MUSIC-LSE) in the framework of multicarrier OFDM SAR imaging for multiple target detection. The necessary conditions for the radar to distinguish the targets were outlined based on a simulation study.

In this paper, the work in [16] is extended to address the problem of SAR image degradation at low SNR (-10 dB) by investigating the effect of OFDM subcarrier selection on the reconstructed SAR image when using a different number of subcarriers. An experimental study is then carried out to validate the initial simulation work in the previous preliminary study by Buhari *et al.* [16]. Steel pipes are used as point targets to image and detect the curvature of the pipes.The results obtained are compared with the LFM SAR and OFDM LSE methods. As direct spatial smoothing is not allowed in MUSIC SAR based systems with a single snapshot since the MUSIC algorithm requires multiple snapshots [27], an improved MUSIC algorithm is utilised for the signal DoA estimation. It is also pertinent to note that MUSIC cannot be directly used as a standalone algorithm in SAR imaging because it does not respond proportionally to the target backscattering power and therefore, the reflectivity information cannot be easily recovered [24], [28]. However, it can be integrated with other SAR algorithms to improve performance. Our approach uses an improved MUSIC algorithm for signal DoA estimation and LSE algorithm for phase history estimation. The algorithms are later integrated to

reconstruct the SAR image and this enhances the resolution of the image.

The remaining part of the paper is organized as follows: Section II describes the SAR system design, signal model, algorithm development and image reconstruction. In Section III, the results and discussion are presented based on simulation and experimental validation of the approach. The conclusion and future work are presented in Section IV.

II. SAR SYSTEM DESIGN, SIGNAL MODEL AND IMAGE RECONSTRUCTION

This section outlines the SAR system geometry, signal model and algorithm development used for the OFDM SAR image reconstruction. A strip map geometry is chosen based on which the OFDM transmit/receive signal model is developed. The proposed MUSIC-LSE algorithm is then formulated to process the received signal and finally reconstructed the image at low SNR.

A. GEOMETRY AND SIGNAL MODEL OF OFDM SAR SYSTEM

Different operational modes exist for the SAR system geometry depending on the targeted application. They include the strip map mode, where the radar moves back and forth within the platform, the spotlight mode, in which the illuminating radar beam is steered continually as the platform moves, and scan mode, where the antenna beam sweeps periodically thereby covering the targeted area [29]. Other approaches include the terrain observation by progressive scans (TOPS) mode used for wide swath coverage and achieved by periodically switching the antenna beam from one sub-swath to another [30]. Two or more operation modes can also be combined to form a hybrid mode operation. In this work, a strip map SAR geometry, shown in Fig. 1, adopted from our previous work in [15] and [16] is used. The radar is mounted on a moving platform and moves from position $-L$ to $+L$. At a given position m, the distance between the SAR platform located at $(u_m, 0)$ and the target positioned at (u_0, y_0) is defined by R_m (called the range). The radial velocity of the SAR platform is denoted V_m. The center of the target area is defined by (u_c, y_c) which corresponds to a broadside target model. As the radar transmits the signals towards the target, the received signal may be in a line of sight or non-line of sight and it thus requires an optimized solution to estimate the location of the target. The phase history can be used to reconstruct the target position. For the signal model, a baseband OFDM signal is used. The target goal is to generate a baseband OFDM waveform for N subcarriers centred at $k*f_1(k = 1, 2, \ldots, N); f_1 = f_s/2N$ and f_s is the OFDM transmitter sampling frequency from the digital to analog converter (DAC). This makes the signal real and discrete, comprising $2N + 1$ samples of the transmitted signal [15]. Using the DAC, the discrete transmitted signal is converted to a continuous time-domain signal $s_t(t)$ and for a given SAR position m, this is given by [25]

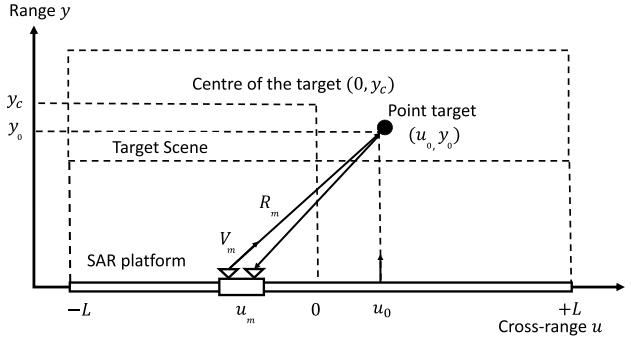

FIGURE 1. SAR system geometry [16].

$$s_{tm}(t) = \frac{1}{M}\sum_{k=1}^{M} S(k)\cdot e^{j\frac{2\pi f_s(k-1)}{M}t}, \quad for \quad 0 \le t \le \frac{N}{f_s} \tag{1}$$

where $M = 2N + 1$, $S(k)$ are real-valued elements of the frequency domain vector $\hat{S}$ which are the frequency points from the DFT arranged in a zero-positive-negative order defined by

$$\hat{S} = [0\ S(1), \ldots, S(N)\ S(N)\ S(N-1), \ldots, S(1)] \tag{2}$$

The reflected signal from the target at the m^{th} SAR position, $s_{rm}(t)$ is given by [26]

$$s_{rm}(t) = \alpha_m s_{tm}\left(t - \frac{2R_m}{c - V_m}\right) \tag{3}$$

where α_m is the reflectivity coefficient of the target. The received signal is then sampled with $(N+1)$ discrete samples to obtain [25]

$$s_{rm}(n) = \frac{\alpha_m}{M}\sum_{k=1}^{M} S(k).e^{j\frac{2\pi(k-1)}{M}\left(n-1+\tau f_s-\frac{2R_m}{c-V_m}f_s\right)}$$
$$n = 1, \cdots, N+1 \tag{4}$$

where τ is the initial sampling time delay.

In a real-life scenario, the received signal is the time lag of the transmitted signal with noise in the form of additive white Gaussian noise (AWGN). To analyse the received signal, the sampled received signal is converted to the frequency domain using DFT, thereby recovering the original number of subcarriers N. The DFT of the received signal at a given SAR position m is given by (details of which can be found in [7], [15], [25])

$$S_{rm} = \frac{\alpha_m}{M}\Upsilon\Phi \tag{5}$$

where

$$\Phi = \begin{bmatrix} e^{-j\frac{\pi\left(\frac{2R_m}{c-V_m}f_s - 1\right)}{M}} \\ \vdots \\ e^{-j\frac{2N\pi\left(\frac{2R_m}{c-V_m}f_s - 1\right)}{M}} \end{bmatrix} \tag{6}$$

$$\Upsilon = \begin{bmatrix} \left(Q_{p,q}S(q+1)\right)_{1,1} & \cdots & \left(Q_{p,q}S(q+1)\right)_{1,2N} \\ \vdots & \ddots & \vdots \\ \left(Q_{p,q}S(q+1)\right)_{N,1} & \cdots & \left(Q_{p,q}S(q+1)\right)_{N,2N} \end{bmatrix} \tag{7}$$

And

$$Q_{p,q} = \begin{cases} \frac{1}{2}\left[M - jtan\left(\frac{\pi(p+q)}{2M}\right)\right], & for \quad p = q \\ \frac{1}{2}\left[M + j\frac{1}{tan\left(-\frac{\pi(p-q)}{2M}\right)}\right], & for \quad p+q = M \\ -\frac{j}{2}\left[tan\left(-\frac{\pi(p-q)}{2M}\right) + tan\left(\frac{\pi(p+q)}{2M}\right)\right], & \\ \quad for \quad p+q = even, \quad p \neq q & \\ \frac{j}{2}\left[\frac{1}{tan\left(\frac{-\pi(p-q)}{2M}\right)} + \frac{1}{tan\left(\frac{\pi(p+q)}{2M}\right)}\right], & \\ \quad for \quad p+q = odd, \quad p+q \neq M & \end{cases} \tag{8}$$

Adding an iid AWGN noise to the received signal, we get

$$\hat{S}_{rm} = S_{rm} + \mathcal{N}_N = \alpha_m \boldsymbol{\Upsilon}\boldsymbol{\Phi} + \mathcal{N}_N \tag{9}$$

where $S_{rm} = MS_{rm}$, S_{rm} is defined in (5) and $\mathcal{N}_N$ is AWGN noise, $\mathcal{N} \sim (0, \sigma_\omega^2)$.

Using the system geometry and the signal model, the target can be reconstructed, as described in the next subsection.

B. SAR IMAGE RECONSTRUCTION USING INTEGRATED MUSIC-LSE ALGORITHM

In this section, the OFDM SAR image reconstruction procedure is outlined, as shown in Fig. 2, and it is based on an integrated MUSIC-LSE algorithm. The algorithm integration offers a robust processing approach which gives a high-resolution image in a dense environment with low SNR (−10 dB). The block diagram started from baseband OFDM signal generation which is converted to the time domain through a DAC. The OFDM signal is used as the transmitted signal and the reflected signal (in time) from the target is sampled and converted to the frequency domain using DFT. This received signal in frequency space is then used to form the range profile reconstruction (RPR) and the cross-range profile reconstruction (CPR). For the RPR, the received signal is a matched filter with a reference transmitted signal.

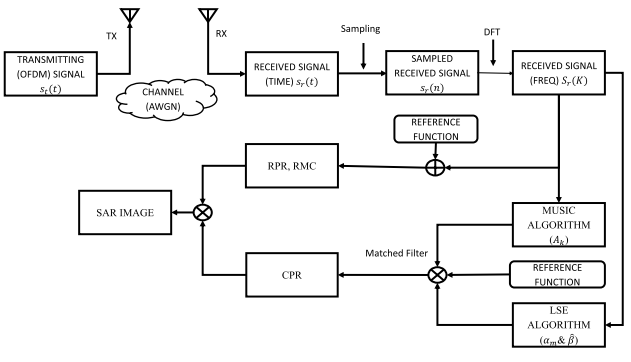

FIGURE 2. Procedure for the OFDM SAR target reconstruction process.

We later apply RMC to correct the migration associated with the range while in the case of the CPR, the received signal is used in both the MUSIC and the LSE algorithm. MUSIC is used to estimate the DoA of the multiple return signals while LSE is used for phase history estimation. The output of the MUSIC (A_k) and the LSE (α_m and $\hat{\beta}$) are matched filtered with a reference transmitted signal to form the CPR. Finally, the SAR image is generated by taking the product of the RPR with the corresponding CPR. The target reconstruction performance is tested in high and low SNR.

1) MUSIC ALGORITHM

In the DoA estimation algorithm, MUSIC is the most popular subspace algorithm used to estimate the signal DoA at the receiver. This is done by decomposing the covariance matrix of the received signal into two subspaces, namely the signal subspace and noise subspace which are orthogonal to each other. The estimation is performed using either of these subspaces under the assumption that the noise in each channel is uncorrelated and hence the covariance matrix is a square matrix with the variance as a diagonal matrix [31]. Given M array elements separated by a distance d, a signal DoA θ, and assuming the received signal to be complex valued in the form $e^{j2\pi f_0 t}$, the received signal at position 1 is given by $s_{r1}(t) = e^{j2\pi f_0 t} = s_r(t)$. At position 2, the received signal is $s_{r2}(t) = s_r(t-\tau) = s_{r1}(t)e^{-j\phi}$, where $\phi = 2\pi d \sin\theta/\lambda_0$; λ_0 is the wavelength. Following the same principle, the total received signal can be expressed using

$$\hat{s}_{rm}(t) = \sum_{i=1}^{m} \alpha(\phi_{i-1}) s_r(t) + n_i(t) \tag{10}$$

where $\alpha(\phi_{i-1}) = [1 \;\; e^{-j\phi} \;\; \ldots \;\; e^{-j(m-1)\phi}]^T$ is the steering vector corresponding to the DoA of the signal at position i, $s_r(t)$ is the incident wave and $n_i(t) = [n_1(t)\; n_2(t) \;\ldots\; n_m(t)]^T$ is the noise subspace.

In the frequency domain, the total received signal can be expressed as

$$\hat{S}_{rm}(k) = \sum_{i=1}^{m} A(k_{i-1}) S_r(k) + N_i(k), \quad k = 1, \ldots K \tag{11}$$

where $\hat{S}_{rm}(k)$ is the received data vector, $N_i(k)$ is the noise vector, and $A(k_{i-1})$ is the steering vector given by $A(k_{i-1}) = [a(1)_0 \;\; a(2)_1 \;\; \ldots \;\; a(K)_{m-1}]^T$ with $a(k_{i-1}) = [1 \; e^{-j2\pi f_2 \phi_1} \;\; \ldots \;\; e^{-j2\pi f_K \phi_{m-1}}]^T$, K is the number of snapshots and m is the number of spatial samples.

In the same way, the M-array principle can be used for SAR configuration by moving the SAR antenna from position 1 to m to create an array-like structure. Hence, to apply MUSIC, the eigenstructure and decomposition of the sample covariance matrix of the return signal are explored. Using (3) as a signal model and considering (10), the SAR received signal is given by

$$\hat{s}_{rm}(t) = \sum_{i=1}^{m} \alpha_i \alpha(\phi_{i-1}) s_t(t-\tau_i) + n_i(t) \tag{12}$$

For the received signal model shown in (9), the received signal using MUSIC in (12) is given by

$$\hat{S}_{rm} = A_k S_r + \mathcal{N}_N = A_k \alpha_m \Upsilon \Phi + \mathcal{N}_N \tag{13}$$

The covariance matrix can be expressed as

$$\begin{aligned} R_{\hat{S}_{rm}\hat{S}_{rm}} &= \mathbb{E}\left\{\hat{S}_{rm}\hat{S}_{rm}^H\right\} \\ &= \mathbb{E}\left\{(A_k S_{rm} + \mathcal{N}_N)(A_k S_{rm} + \mathcal{N}_N)^H\right\} \\ R_{\hat{S}_{rm}\hat{S}_{rm}} &= A_k R_{s_{tm}s_{tm}} {A_k}^H + \sigma_N^2 I_N \end{aligned} \tag{14}$$

where $\mathbb{E}$ is the expected value, H is the the conjugate response called the Hermitian, $R_{s_{tm}s_{tm}}$ is the transmitted signal correlation matrix, σ_N^2 is the variance of the AWGN vector $\mathcal{N}_N$, A_k is the steering vector given by $A(k_i) = [a_1\ a_2\ \ldots\ a_K]$ and I_N is an identity matrix.

From (14), it can be seen that the MUSIC algorithm depends on the signal covariance matrix $R_{s_{tm}s_{tm}}$ which is non-singular, the steering vector A_k which is linearly independent and the noise covariance matrix given by $\sigma_N^2\ I_N$. The covariance matrix can be estimated from (14) using

$$\hat{R}_{\hat{S}_{rm}\hat{S}_{rm}} = \frac{1}{K}\sum_{k=1}^{K} \hat{S}_{rm}(k)\hat{S}_{rm}(k)^H \tag{15}$$

where K is the number of samples of the received signal.

Using (15), in order to develop the covariance matrix, multiple samples of the received signals are needed to satisfy the requirements of the MUSIC algorithm. However, for our system, a single snapshot is used, which makes the covariance matrix singular and correlated and therefore the MUSIC algorithm fails. As direct spatial smoothing is not allowed and in order to effectively use MUSIC in our model, an improved spatial smoothing method is needed before applying MUSIC to (14), detail of which can be found in [26]. This is achieved by defining new window elements v_i such that the initial elements v_1 and v_2 are less than the signal dimensions. The initial window element dimension v_1 is used as the reference and later the $v_1 * v_2$ received signal matrix array is vectorised using $vec(v_1 * v_2)$. The improved covariance matrix becomes

$$\hat{R}_{\hat{S}_{rm}\hat{S}_{rm}} = \frac{1}{2K}\sum_{k=1}^{K}\left(Q\hat{R}_{\hat{S}_{rm}\hat{S}_{rm}}(k)^H Q + \hat{R}_{\hat{S}_{rm}\hat{S}_{rm}}(k)\right) \tag{16}$$

where Q is an anti-diagonal matrix.

Equation (16) ensures that, by using the improved spatial smoothing, there is a guarantee that the covariance matrix is a diagonal matrix and uncorrelated. Therefore, the MUSIC algorithm can be applied using the signal and the noise subspace defined in (14). The improved MUSIC spatial spectrum is given by (17) [25]. The MUSIC algorithm procedure is described in Algorithm 1.

$$P_{MUSIC} = \frac{1}{\|A_k^H \mathcal{N}_N \mathcal{N}_N^H A_k\|} = \frac{A_k^H A_k}{A_k^H \mathcal{N}_N \mathcal{N}_N^H A_k} \tag{17}$$

Algorithm 1 Multiple Signal Classification (MUSIC)

Input: Received signal in frequency space, $\hat{S}_r$ for all values of m.

1: Using $\hat{S}_{rm}$, form the covariance matrix $R_{\hat{S}_{rm}\hat{S}_r}$ using (14).
2: Decompose $R_{\hat{S}_{rm}\hat{S}_{rm}}$ into signal subspace $A_k R_{s_{tm}s_{tm}} {A_k}^H$ and noise subspace $\mathcal{N}_N I_N$.
3: Estimate $\hat{R}_{\hat{S}_{rm}\hat{S}_{rm}}$ using improved spatial smoothing. This makes the $\hat{R}_{\hat{S}_{rm}\hat{S}_{rm}}$ uncorrelated and non-singular.
4: Recompute $\hat{R}_{\hat{S}_{rm}\hat{S}_{rm}}$ using (16).
5: Form the matrix of the steering vector A_k and this estimates the signal DoA.
6: Compute P_{MUSIC} using (17).

Output: Steering vector A_k and P_{MUSIC}.

2) LSE ALGORITHM

LSE is one of the popular methods used in parameter estimation between an observed value and its true or expected value. It is achieved by estimating the square of the difference between the two values using the L^2-norm minimisation technique [31]. In this paper, LSE is used to estimate the phase history using the received signal in (9). Using the data model, the L^2-norm is formulated to estimate the residual between the received sample and the data model β using [25]

$$R(\beta, \hat{S}_{rm}) = \left\|\hat{S}_{rm} - \alpha_m \boldsymbol{\Upsilon\Phi}\right\|^2 \tag{18}$$

Through the minimisation of (18), an estimate of β can be obtained for a known value of α_m. However, in real life, the value of α_m is unknown and needs to be determined by solving equation (18) (details of the derivation can be found in [7]).
Expanding (18) yields

$$R(\beta, \hat{S}_{rm}) = \left(\hat{S}_{rm}^H - (\alpha_m \boldsymbol{\Upsilon\Phi})^H\right)\left(\hat{S}_{rm} - \alpha_m \boldsymbol{\Upsilon\Phi}\right) \tag{19}$$

The value for α_m can then be found by taking the partial derivative of (19) and equating the result to zero to get

$$\alpha_m = \frac{|\hat{S}_{rm}^H \boldsymbol{\Upsilon\Phi}|}{\boldsymbol{\Phi}^H \boldsymbol{\Upsilon}^H \boldsymbol{\Upsilon\Phi}} \tag{20}$$

The phase history estimate for the case of an unknown value of α_m becomes [25]

$$\hat{\beta} = \arg\max_{\beta} \left\|\frac{\hat{S}_{rm}^H \boldsymbol{\Upsilon\Phi}}{|\boldsymbol{\Upsilon\Phi}|}\right\| \tag{21}$$

Equation (21) gives an estimate of the phase history which can be used for the image reconstruction process in the cross-range domain. The LSE algorithm is described in algorithm 2.

3) SAR IMAGE RECONSTRUCTION

The standard procedure in SAR imaging is to combine RPR and CPR to form the image. The CPR can be formed by

Algorithm 2 Least Square Estimation (LSE)

Input: Received signal in frequency space, $\hat{S}_r$ for all values of m.

1: Form the L^2norm to using $R(\beta, \hat{S}_{rm})$.
2: Using (20), find an estimate for α_m.
3: Compute an estimate of the phase history β using (21). This estimates the Doppler shift at each given SAR position m.

Output: Target reflectivity α_m and phase history β.

matched filtering the phase of the single complex sinusoid at a given SAR position m with a reference function given by

$$R_{CPR}(u_m) = \left(e^{-j2\pi(K_m-\tau)\frac{f_s}{M}}\right) \otimes \left(e^{-j2\pi\frac{\hat{\beta}_m}{M}}\right) \tag{22}$$

where $\otimes$ is the cross-correlation operator and K_m is the round trip delay between the target and the radar.

The RPR at a given cross-range position u_m is derived by matched filtering the reflected signal with a reference transmitted signal in frequency space given by [25]

$$R_{RPR}(t) = \mathcal{F}^{-1}(S_{ref} \otimes \hat{S}_r) \tag{23}$$

where $\mathcal{F}^{-1}$ is the inverse Fourier transform, S_{ref} is the reference transmitted signal in the frequency domain which is zero padded to achieve the desired length of K samples and S_r is the received signal from (9) upsample to the entire length of K.

Moreover, because of the fact that the radar moves along the cross-range position, the RPR in (23) suffers from range ambiguity which results in range migration (RM). This can be solved by using the cross-range information to account for the migration through a process known as range migration correction (RMC), details of which can be found in our previous work [1], [7]. The RMC in [1] is utilised and the $R_{RPR}(t)$ in (23) is updated with the frequency compensation term. This is later converted to the range domain using $t = 2y/c$. To form the 2D SAR image, the product of each RPR is taken with the corresponding CPR to obtain [25]

$$I_{SAR} = R_{RPR}(y_m) \cdot R_{CPR}(u_m) \tag{24}$$

III. RESULTS AND DISCUSSION

In this section, the results obtained based on the method described in Section II are presented and analysed. We start with the image reconstruction using the integrated MUSIC-LSE algorithm to enhance the quality of the image at low SNR. Simulation results evaluate the quality of the reconstructed image using three performance indicators of root mean square error (RMSE), cumulative side lobe levels and main lobe width. Finally, the behaviour of the reconstructed SAR image is investigated by varying the OFDM subcarriers for optimal design. Three sets of results are used for comparison, namely the LFM-based results, OFDM LSE-based results (later termed LS for simplicity) and the OFDM MUSIC-LSE (later termed LS-MU) results. Experimental validation is carried out using two steel pipes as targets to image and detect the pipe curvatures.

A. SIMULATION RESULTS FOR MULTICARRIER SAR SYSTEM

The parameters used for the simulation are set to the following values (typical of normal conventional S-BAND and X-BAND SAR): Number of subcarriers $N = 4, 8$ and 16; Target center $y_c = 1$ m; Bandwidth $BW = 4$ GHz; Moving length $L = 1$ m; pulse repetition frequency, $f_{PRF} = 35$ Hz; sampling frequency, $f_s = 1$ GHz; radial speed of the SAR, $V_u^{SAR} = 35$ m/s; step size used $\Delta u = 301$.

1) OFDM SUBCARRIER SELECTION

For different number of subcarriers used in the target reconstruction, there is a need to know the associated effects. To do this, different target positions were tried both for a single and for multiple targets using $N = 8$ and the results are shown in Fig. 3. For the detection of the target, the cross-range information can suffice. Fig. 3 shows that both of the methods used successfully detected the target position. The LS-MU gives a better side lobe level compared to the LS case. This is because, for the LS-MU, the signal DoA was estimated before applying the LS estimation. In a low SNR condition, the side lobes interfere with the main lobe, resulting in target degradation. Therefore, there is a need to investigate the target reconstruction accuracy and the best choice for the number of subcarriers N by varying the SNR from low to high. This can be done using the RMSE to measure the error between the estimated target position $\hat{u}_{m_0}$ and the actual target location u_0 for all the SAR positions m, the cumulative side-lobe level ρ_s found by taking the ratio of the areas under the simulated and

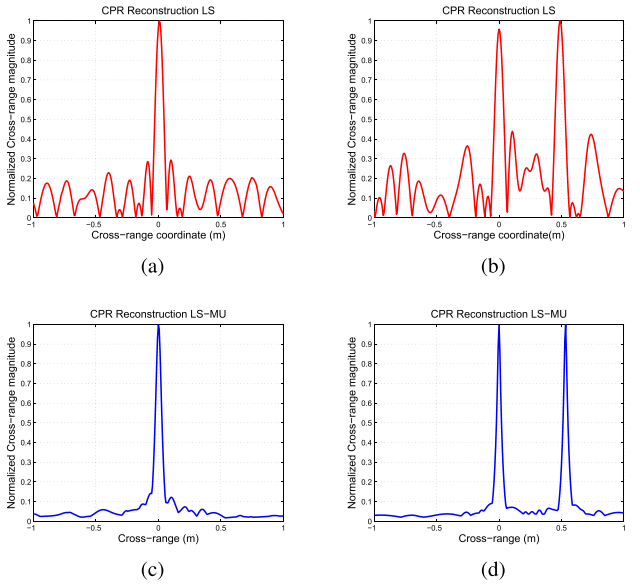

FIGURE 3. Normalised CPR reconstruction for target(s) (a) LS at $u_0 = 0$ m. (b) LS at $u_{01} = 0$ m, $u_{02} = 0.5$ m. (c) LS-MU at $u_0 = 0$ m. (d) LS-MU at $u_{01} = 0$ m, $u_{02} = 0.5$ m.

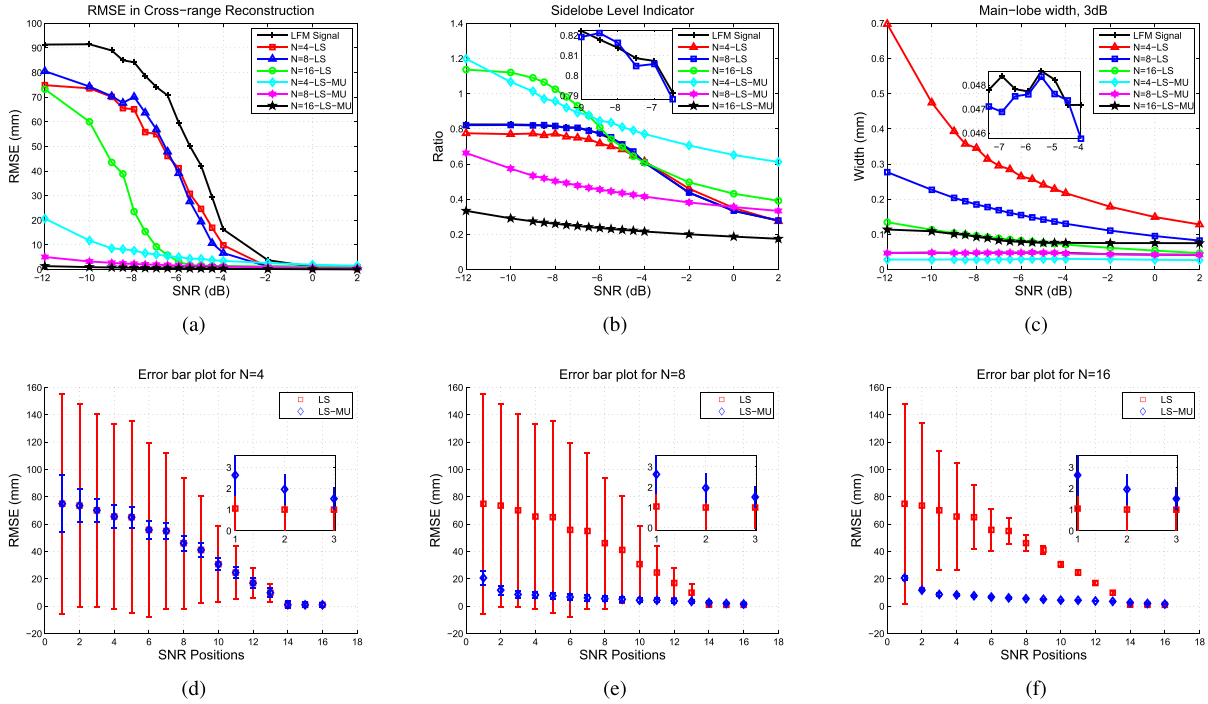

FIGURE 4. Performance of the CPR (a-c) and error bar plots (d-f) (a) RMSE. (b) Cumulative side lobe level (c) Main lobe width. (d) Error bar plot for $N = 4$. (e) Error bar plot for $N = 8$. (f) Error bar plot for $N = 16$.

the ideal CPR and the main lobe width (the 3 dB beam width of the CPR main lobe) to measure the quality of cross-range resolution. Using these performance indicators, the quality of the reconstructed target (CPR) is measured and evaluated. The subcarriers are assumed to be ON (ones) and the results are compared with an LFM signal at a frequency of $f_0 = f_s/17$ corresponding to the fundamental frequency of the reference function for the case of $N = 8$ given by $f_s/(2N + 1)$). The results are shown in Fig. 4.

From Fig. 4, it can be observed that the RMSE decreases as the number of subcarriers increases. The LS and LS-MU perform better than the LFM case for both cases of N. This is expected because, as the value of N increases, more data are available for the estimation process which improves the reconstruction accuracy. From Fig. 4(a), two regions of interest were observed namely low and medium SNR regions. The low SNR region is the region between 10 dB to 2 dB and because of the noise and interference in this region, higher values of N give the worst result in the case of LS estimation. This means that choosing a lower value of N is the optimal choice. However, this is not the case for LS-MU as it still performs well and this is attributed to the contribution of the improved MUSIC.

In the medium SNR, the RMSE results of $N = 16$ perform better (fewer errors) than the cases of $N = 4$ and $N = 8$ for both LS and LS-MU cases whilst still giving a lower error estimate than the case of LFM. At an SNR of 2 dB, all the three methods give the same level of performance which is expected because, in this condition, only one carrier is enough to estimate the target position. In terms of the errors made, error bars shown in Fig. 4(d-f) were used to compare the estimation accuracy for LS and LS-MU, which comparison showed that a lower error is made in LS-MU compared to the LS case. However, there is a trade-off between increasing the number of subcarriers and the main lobe width of the CPR, as observed in Fig. 4(c). This is because, as the number of subcarriers increases, the main lobe of the CPR becomes wider for the LS case. This can be explained by looking at the fundamental frequency f_s/M which decreases as N increases. As a result, the main lobe becomes wider and this explains why $N = 8$ gives a better result for the main lobe width compared to $N = 16$. However, this is not noticeable in the LS-MU case because of the sharp peak of the main lobe of the LS-MU.

The computational cost and reconstruction accuracy of the approach is influenced by the SNR requirements in low (-10 dB) and medium (2 dB) SNR regions, as illustrated in Table 1. It can be seen that, as the number of subcarriers increases, the error estimation in the reconstruction of the target position reduces, as observed from the values of the RMSE and CSL. This is because the higher the number of subcarriers, the more data are available for the estimation. However, looking at the main lobe width, as the number of subcarriers increases, the main lobe becomes wider. Thus, it can be said that the higher the number of subcarriers, the better the quality of the reconstructed target at the cost of having a wider main lobe. In terms of computational cost, LFM is less complex compared to OFDM SAR, as observed

TABLE 1. Comparison between different methods in low and high SNR regions.

Performance Indicators	Low SNR				High SNR			
	LFM	OFDM			LFM	OFDM		
		N=4	N=8	N=16		N=4	N=8	N=16
RMSE (mm)	91.00	12.00	4.00	1.00	0.03	0.03	0.03	0.03
Cumulative side lobe level	0.82	1.10	0.57	0.27	0.29	0.61	0.33	0.17
Main lobe width (mm)	0.50	0.30	0.50	1.10	0.50	0.20	0.50	0.80
Computational time (s)	286.60	198.88	287.95	386.42	281.11	193.00	281.90	380.50

by the time taken to reconstruct the target. This is because OFDM fully utilises the bandwidth (which is a limited resource in radar) by using more subcarriers, thereby giving more data for the estimation and this enhances the accuracy of the reconstructed target. Due to increase in computational time as a result of fully utilising the whole of the bandwidth, compressive sensing can be used to reduce the computational time. This point is highlighted as part of our future work.

2) SAR IMAGE RECONSTRUCTION

After investigating the selection of the optimal number of subcarriers, the SAR image is reconstructed using the method described in subsection (II, B, 3) and a low SNR of -10 dB is chosen to show the capability of the LS-MU in comparison to the LS case. The number of subcarriers used is $N = 128$. Two targets are used to observe the necessary conditions for the radar to distinguish the targets. These conditions are given by [25]

$$\begin{cases} d_R \geq \Delta R = \frac{c}{2B} \\ d_C \geq \delta x = \frac{L_a}{2} \end{cases} \tag{25}$$

where B is the bandwidth, c is the speed of light and L_a is the antenna aperture size.

The bandwidth used for the simulation is 4 GHz. This translates to a range resolution of $\Delta R = 0.375$ m. For $L_a = 2$ m, the cross-range resolution is given by $\delta x = L_a/2 = 30/2 = 1$ cm. Two cases were considered for the target reconstruction. The first case is when the distance between the two targets in the range and cross-range is less than the radar range and cross-range resolution. The targets are located at ($u_{01} = 0$ m, and $u_{02} = 0.1$ m) both at a range position of $y_0 = 1$ m (for simplicity). The results are shown in Fig. 5 (a-d). It can be seen that, whereas the LS case imaged the two targets together as one large target, the LS-MU case separated the two targets with some ghost targets around the main target. This happens because we are operating at below the radar range and cross-range resolutions. However, with improvement in the SAR signal processing, it is possible for the radar to distinguish the targets even below the radar range and cross-range resolutions. The second case occurs when both the two conditions are met. The targets are located at ($u_{01} = 0$ m, and $u_{02} = 0.5$ m) and the results are shown in Fig. 5 (e-h). It can be seen that both methods successfully separated the targets, however, the LS-MU has a higher image resolution compared to the LS case [7].

B. SAR EXPERIMENTAL VALIDATION

To validate the simulation results shown in section III(A), the experimental set-up in Fig. 6 is used. This consists of a vector network analyser (VNA) that is connected to two pairs of horn antennae via RF cables at one end and to a workstation PC via a general purpose interface bus (GBIP) at the other end. The horn antennae are mounted on a movable platform (rail 2 m long). An ustepper controller board is used to control the antenna movement along the rail. The antennae acquire SAR phase history data of the target scene at evenly spaced increments across the platform and this is achieved by recording the S_{21} scattering parameters. Port 1 of the VNA is used as the transmitter and port 2 as the receiver. The reflected signal (using S_{21} parameter) is recorded on the VNA and the result obtained is analysed in MATLAB. The design parameters are shown in Table 2. Steel metal pipe samples with diameter $d = 100$ mm and length $l = 600$ mm are used as point targets. The targeted goal is to image and detect the curvature of the pipe sample as point target. The distance between the two metal pipes is defined by the radar range resolution. These samples were used to show the capability of the LS-MU approach in detecting curvatures in pipes. It can also be extended in detecting defects in the pipes by imaging the whole of the pipe.

TABLE 2. SAR Experimental Parameters.

S/N	Parameter	Value
1	Antenna Type	Horn (1-18 GHz)
2	Operating Frequency	$2-6$ GHz
3	Bandwidth	4 GHz
4	Number of points	128
5	Rail length	2 m (step size 22)
6	Range resolution	0.375 m
7	Cross-range resolution	0.1 m

Based on the experimental set-up and as with the simulation results, single and multiple targets scenarios were considered. For the single target scenario, the target was placed at ($u_{01} = 0$ m, $y_{01} = 0.95$ m) and the results are shown in Fig. 7. Fig. 7(a) shows the raw SAR image data captured after the rail scan. It can be seen that because of the movement of the radar, a range migration has occurred in the raw data. This can be corrected using the cross-range information to account for the migration through a process known as RMC,

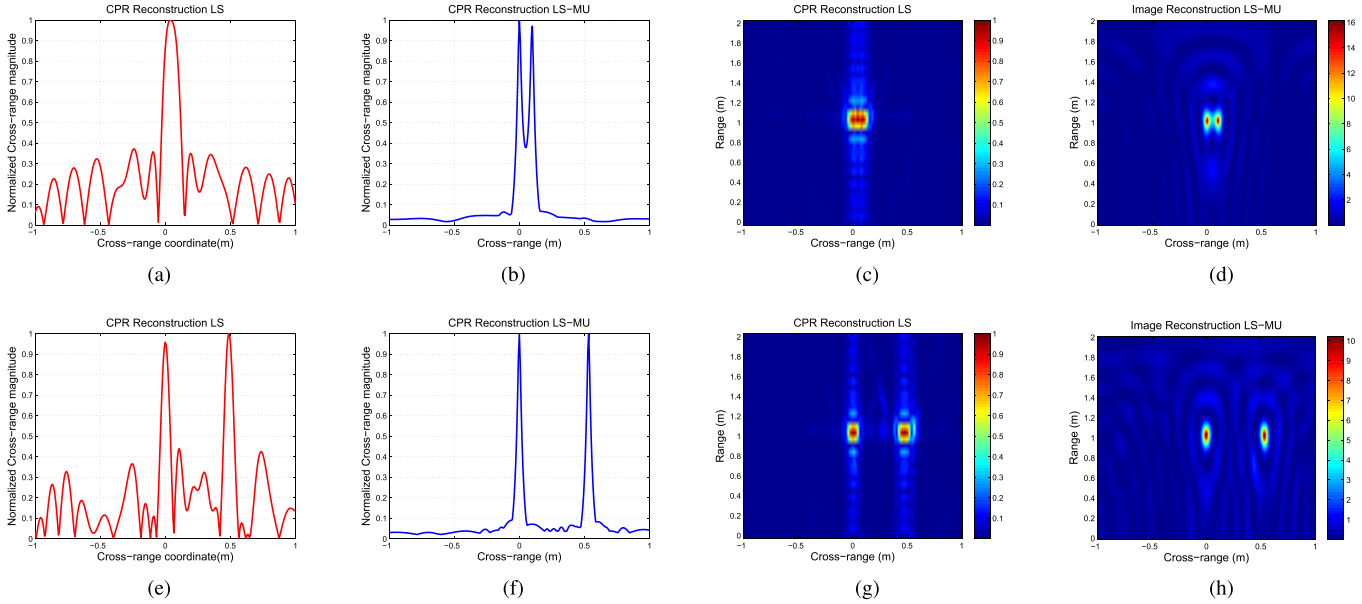

FIGURE 5. Target reconstruction for $d_R < \Delta R$ and $d_C < \delta x$ (a-d) and $d_R \geq \Delta R$ and $d_C \geq \delta x$ (e-h). (a) CPR for LS case. (b) CPR for LS-MU case. (c) SAR image for LS case. (d) SAR image for LS-MU case. (e) CPR for LS case. (f) CPR for LS-MU case. (g) SAR image for LS case. (h) SAR image for LS-MU.

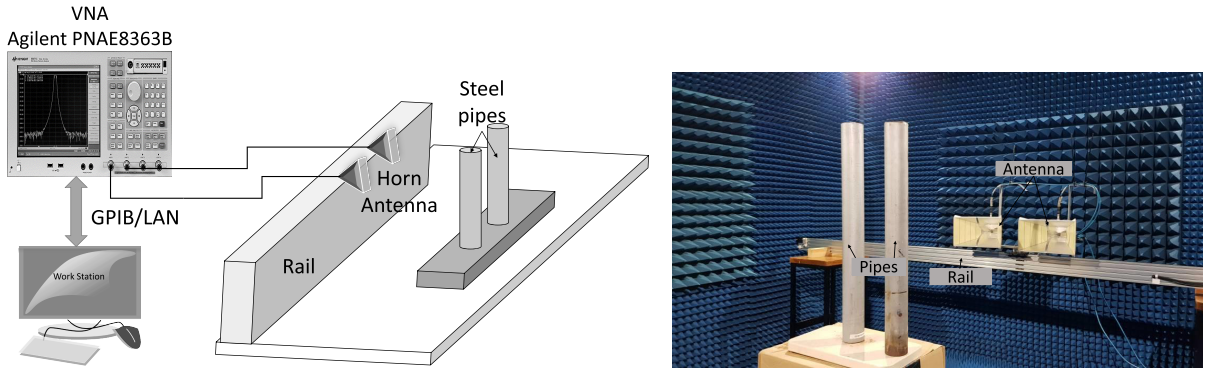

FIGURE 6. Overall experimental SAR design set-up. (a) Schematic of the SAR experimental set-up. (b) Target scene inside the anechoic chamber.

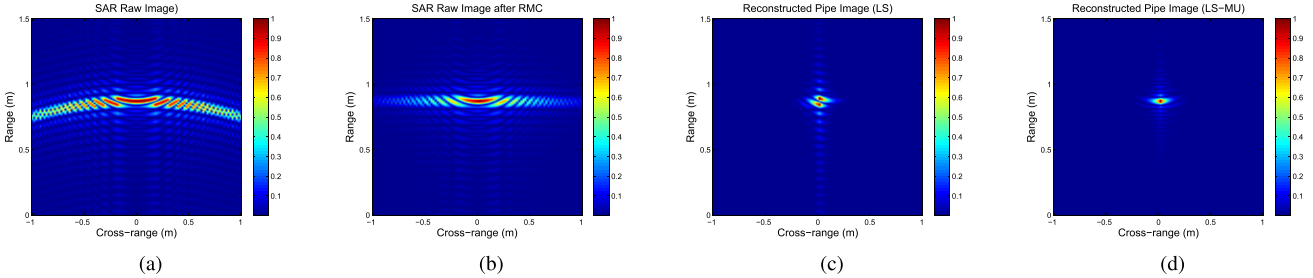

FIGURE 7. Experimental SAR image reconstruction. (a) SAR raw image. (b) SAR raw image after RMC. (c) Reconstructed SAR image (LS). (d) Reconstructed SAR image (LS-MU).

details of which can be found in our previous work [1]. The result is shown in Fig. 7(b). The reconstructed SAR image of the pipe is shown in Fig. 7(c-d). It can be seen that the image from LS-MU gives a better image compared to the LS image. Also, the reconstructed image shows that the LS-MU approach detects the position and the curvature of the pipe

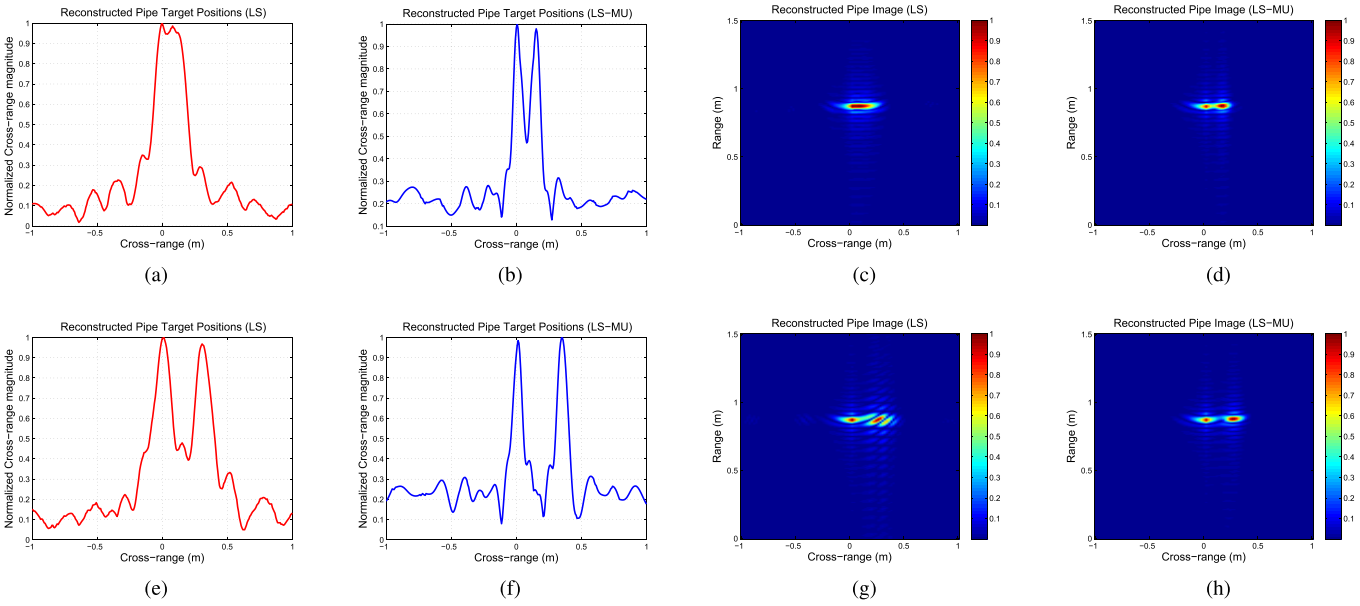

FIGURE 8. Multiple pipes image reconstruction process for $d_R < \Delta R$ and $d_C < \delta x$ (a-d) and $d_R \geq \Delta R$ and $d_C \geq \delta x$ (e-h). (a) CPR for LS case. (b) CPR for LS-MU case. (c) SAR image for LS case. (d) SAR image for LS-MU case. (e) CPR for LS case. (f) CPR for LS-MU case. (g) SAR image for LS case. (h) SAR image for LS-MU.

whereas the LS approach only detects the position of the pipe without the curvature shown. For multiple targets, two targets are used to test the two conditions for the radar to distinguish the two targets. Case I is when none of the conditions are met and the targets are placed at ($u_{01} = 0$ m, $y_{01} = 0.9$ m) and ($u_{02} = 0.1$ m, $y_{02} = 0.9$ m). Case II is when either of the two conditions is satisfied and the targets are located at ($u_{01} = 0$ m, $y_{01} = 0.9$ m) and ($u_{02} = 0.38$ m, $y_{02} = 0.9$ m). The results are shown in Figure 8. In both the two cases, the LS-MU gives a better image and still resolve the two metal pipes even below the radar range resolution compared to the LS image. This shows the capability of the technique.

To further evaluate the quality of the reconstructed images and the estimation accuracy of the two methods, the SNR and contrast-to-noise ratio (CNR) were computed for the SAR images shown in Fig. 7 and 8 respectively. The SNR of the image is calculated using [32]

$$SNR = 20log_{10}\left|\frac{\mu_{ROI}}{\sigma_{ROI}}\right| \tag{26}$$

where μ_{ROI} is the mean and σ_{ROI} is the standard deviation of the image region of interest. The CNR measures the contrast of the image and is given by

$$CNR = 20log_{10}\frac{2(\mu_{ROI} - \mu_B)^2}{\sigma_{ROI}^2 + \sigma_B^2} \tag{27}$$

where μ_B and σ_B are the mean and the standard deviation of the background image.

Using the two evaluation parameters, the images from the two approaches were fairly compared and the SNR and CNR values are presented in Table 3. From the table, it can be observed that LSE-MU gives higher SNR and higher CNR compared to LS method. Hence we can conclude that estimating the signal DoA of the SAR received signal and later applying the LSE algorithm improves the detection as well as the imaging capability of the SAR significantly.

TABLE 3. SNR and CNR values for the reconstructed pipe images.

Method	SNR (dB)	CNR (dB)
LS Single Pipe	6.40	17.11
LS-MU Single Pipe	7.04	19.06
LS for Case I (2 pipes)	6.57	23.02
LS-MU for Case I (2 pipes)	7.10	29.95
LS for Case II (2 pipes)	7.03	28.63
LS-MU for Case II (2 pipes)	8.81	36.90

IV. CONCLUSION

This paper proposed an integrated MUSIC-assisted LSE (MUSIC-LSE) algorithm for multicarrier SAR image reconstruction which gives high-resolution images in low SNR environments. An improved MUSIC algorithm was used for signal DoA estimation and the LSE algorithm for phase history estimation. Three performance indicators, namely RMSE, main lobe width and cumulative side lobe levels, were used to measure and evaluate the strength of the approach through simulation studies. These indicators were also used to investigate the effect of OFDM subcarrier selection on the reconstructed SAR image and it was observed that, as the number of subcarriers increases, the accuracy of the reconstructed target improves at the cost of having a wider main lobe. Experimental validation of the MUSIC-LSE approach was carried out using two steel pipes to image

and detect the curvature of the pipes as point targets.The results obtained show that the MUSIC-LSE approach gives a higher-resolution image in high and low SNR (−10 dB) SNR environments compared to the LFM and OFDM-LSE cases. This is a significant improvement compared to other methods that achieved 5 dB and 2 dB. In addition, the SNR and the CNR values of the MUSIC-LSE reconstructed pipe images are higher compared to the LSE reconstructed images. The MUSIC-LSE approach also shows that it is possible for a radar to distinguish the two steel pipes even below the radar range and cross-range resolutions.

In future, further experimental validation, including using dedicated samples can be investigated on not only detecting the pipes curvature but also the structural health status e.g. corrosion and crack condition using better reconstructed images and their near-far field characteristics [33].

REFERENCES

[1] M. D. Buhari and A. H. Muqaibel, "SAR multiple targets imaging using UWB OFDM signals," in *Proc. IEEE 9th Int. Symp. Commun. Syst., Netw. Digital Signal Process. (CSNDSP)*, Jul. 2014, pp. 485–490.

[2] Y. Huang, G. Liao, J. Xu, and D. Yang, "MIMO SAR OFDM chirp waveform design and GMTI with RPCA based method," *Digit. Signal Process.*, vol. 51, pp. 184–195, Apr. 2016.

[3] G. Jia, M. Buchroithner, W. Chang, and X. Li, "Simplified real-time imaging flow for high-resolution FMCW SAR," *IEEE Geosci. Remote Sens. Lett.*, vol. 12, no. 5, pp. 973–977, May 2015.

[4] J. J. M. de Wit, A. Meta, and P. Hoogeboom, "Modified range-Doppler processing for FM-CW synthetic aperture radar," *IEEE Geosci. Remote Sens. Lett.*, vol. 3, no. 1, pp. 83–87, Jan. 2006.

[5] E. C. Zaugg and D. G. Long, "Generalized frequency-domain SAR processing," *IEEE Trans. Geosci. Remote Sens.*, vol. 47, no. 11, pp. 3761–3773, Nov. 2009.

[6] D. S. Garmatyuk, "Simulated imaging performance of UWB SAR based on OFDM," in *Proc. IEEE Int. Conf. Ultra-Wideband*, Sep. 2006, pp. 237–242.

[7] D. Garmatyuk and M. Brenneman, "Adaptive multicarrier OFDM SAR signal processing," *IEEE Trans. Geosci. Remote Sens.*, vol. 49, no. 10, pp. 3780–3790, Oct. 2011.

[8] T. Zhang, X.-G. Xia, and L. Kong, "IRCI free range reconstruction for SAR imaging with arbitrary length OFDM pulse," *IEEE Trans. Signal Process.*, vol. 62, no. 18, pp. 4748–4759, Sep. 2014.

[9] D. Laurent, F. Matthew, M. Nicholas, P. Jack, and Y. Lexing, "A butterfly algorithm for synthetic aperture radar imaging," *SIAM J. Img. Sci.*, vol. 5, no. 1, pp. 203–243, 2012.

[10] L. Huang, X. Qiu, D. Hu, B. Han, and C. Ding, "Medium-earth-orbit SAR focusing using range Doppler algorithm with integrated two-step azimuth perturbation," *IEEE Geosci. Remote Sens. Lett.*, vol. 12, no. 3, pp. 626–630, Mar. 2015.

[11] H. Xie *et al.*, "Fast factorized backprojection algorithm for one-stationary bistatic spotlight circular SAR image formation," *IEEE J. Sel. Topics Appl. Earth Observ. Remote Sens.*, vol. 10, no. 4, pp. 1494–1510, Apr. 2017.

[12] H. Shi, Q. Zhou, X. Yang, and Q. Lian, "SAR imaging method for sea scene target based on improved phase retrieval algorithm," *J. Syst. Eng. Electron.*, vol. 27, no. 6, pp. 1176–1182, Dec. 2016.

[13] L. Yang, L. Zhao, S. Zhou, and G. Bi, "Sparsity-driven SAR imaging for highly maneuvering ground target by the combination of time-frequency analysis and parametric Bayesian learning," *IEEE J. Sel. Topics Appl. Earth Observ. Remote Sens.*, vol. 10, no. 4, pp. 1443–1455, Apr. 2017.

[14] X.-Y. Pan *et al.*, "Extraction of micro-doppler frequency from HRRPs of rotating targets," *IEEE Access*, vol. 5, pp. 26162–26174, 2017.

[15] D. Garmatyuk, "Cross-range SAR reconstruction with multicarrier OFDM signals," *IEEE Geosci. Remote Sens. Lett.*, vol. 9, no. 5, pp. 808–812, Sep. 2012.

[16] M. D. Buhari, G. Y. Tian, R. Tiwari, and A. H. Muqaibel, "Adaptive OFDM subcarrier design for SAR cross-range profile reconstruction," in *Proc. IEEE Int. Conf. Students Appl. Eng. (ICSAE)*, Oct. 2016, pp. 485–490.

[17] J. Bosse, O. Krasnov, and A. Yarovoy, "Direct target localization with an active radar network," *J. Signal Proces.*, vol. 125, pp. 21–35, Aug. 2016.

[18] O. A. Oumar, M. F. Siyau, and T. P. Sattar, "Comparison between MUSIC and ESPRIT direction of arrival estimation algorithms for wireless communication systems," in *Proc. IEEE Int. Conf. Future Generat. Commun. Technol.*, Dec. 2012, pp. 99–103.

[19] M. L. Bencheikh and Y. Wang, "Joint DOD-DOA estimation using combined ESPRIT-MUSIC approach in MIMO radar," *Electron. Lett.*, vol. 46, no. 15, pp. 1081–1083, 2010.

[20] W. Zheng, X. Zhang, and J. Shi, "Sparse extension array geometry for DOA estimation with nested MIMO radar," *IEEE Access*, vol. 5, pp. 9580–9586, 2017.

[21] H. O. Bektas, O. Ozdemir, M. Orhan, and A. S. Turk, "An experimental investigation of F-K migration and SAR algorithm using beam space MUSIC for UWB through-the-wall imaging," in *Proc. IEEE Radar Methods Syst. Workshop (RMSW)*, Sep. 2016, pp. 70–75.

[22] L. Zhang *et al.*, "Resolution enhancement for inversed synthetic aperture radar imaging under low SNR via improved compressive sensing," *IEEE Trans. Geosci. Remote Sens.*, vol. 48, no. 10, pp. 3824–3838, Oct. 2010.

[23] A. Liao, Z. Gao, Y. Wu, H. Wang, and M.-S. Alouini, "2D unitary ESPRIT based super-resolution channel estimation for millimeter-wave massive MIMO with hybrid precoding," *IEEE Access*, vol. 5, pp. 24747–24757, 2017.

[24] Y.-S. Cho, H.-K. Jung, C. Cheon, J. So, and Y.-S. Chung, "Range-cell-focusing algorithm combined with enhanced MUSIC for close target imaging," *IEEE Geosci. Remote Sens. Lett.*, vol. 13, no. 8, pp. 1109–1113, Aug. 2016.

[25] M. D. Buhari, G. Y. Tian, R. Tiwari, R. Sutthaweekul, and A. H. Muqaibel, "OFDM SAR multiple targets image reconstruction using MUSIC-LSE algorithm," in *Proc. IEEE Int. Workshop Compressed Sens. Theory Appl. to Radar, Sonar Remote Sens. (CoSeRa)*, Sep. 2016, pp. 42–46.

[26] C. Chen and Z. Xiaoling, "A new super-resolution 3D-SAR imaging method based on MUSIC algorithm," in *Proc. IEEE RadarCon (RADAR)*, May 2011, pp. 525–529.

[27] B. Koh, S. Choi, and J. Chun, "A SAR autofocus technique with music and golden section search for range bins with multiple point scatterers," *IEEE Geosci. Remote Sens. Lett.*, vol. 12, no. 8, pp. 1600–1604, Aug. 2015.

[28] G. Krieger, "MIMO-SAR: Opportunities and pitfalls," *IEEE Trans. Geosci. Remote Sens.*, vol. 52, no. 5, pp. 2628–2645, May 2014.

[29] X. Liang, H. Zhang, G. Fang, S. Ye, and T. A. Gulliver, "An improved algorithm for through-wall target detection using ultra-wideband impulse radar," *IEEE Access*, vol. 5, pp. 22101–22118, 2017.

[30] X. Wang, B.-J. Kim, and H.-G. Ryu, "DOA estimation By ESPAR antennas using fourth-order MUSIC algorithm," in *Proc. USNC-URSI Radio Sci. Meeting (Joint AP-S Symp.)*, 2014, p. 203.

[31] H. Song, W.-A. Zhang, L. Yu, and L. Shi, "Multi-sensor-based aperiodic least-squares estimation for networked systems with transmission constraints," *IEEE Trans. Signal Process.*, vol. 63, no. 9, pp. 2349–2363, May 2015.

[32] Z. Liu, C. Huang, and J. Luo, "A systematic investigation of lateral estimation using various interpolation approaches in conventional ultrasound imaging," *IEEE Trans. Ultrason., Ferroelect., Freq. Control*, vol. 64, no. 8, pp. 1149–1160, Aug. 2017.

[33] Q. Cheng, A. Alomainy, and Y. Hao, "Near-field millimeter-wave phased array imaging with compressive sensing," *IEEE Access*, vol. 5, pp. 18975–18986, 2017.

MOHAMMED D. BUHARI (GS'16) received the B.Eng. degree in electrical and electronic engineering from Abubakar Tafawa Balewa University, Bauchi, Nigeria, in 2008, and the M.Sc. degree in telecommunications engineering from the King Fahd University of Petroleum and Minerals, Saudi Arabia, in 2014. He is currently pursuing the Ph.D. degree in electrical and electronic engineering with Newcastle University, U.K.

His research interests include OFDM SAR signal and image processing, SAR inspection for NDT&E applications, weapon detection, and through-the-wall radar imaging.

GUI YUN TIAN received the B.Sc. and M.Sc. degrees from the University of Sichuan, Chengdu, China, in 1985 and 1988, respectively, and the Ph.D. degree from the University of Derby, Derby, U.K., in 1998. He is currently a Professor of sensor technologies with the School of Electrical and Electronic Engineering, Newcastle University, U.K. His main research interests include electromagnetic sensors, sensor array and sensor network, electromagnetic non-destructive evaluation, advanced signal processing, and integrative systems and applications.

He has coordinated several research projects from the Engineering and Physical Sciences research Council, Royal Academy of Engineering and FP7. He has also good collaboration with leading industrial companies such as airbus, rolls royce, BP, nPower, network rail, and TWI.

RAJESH TIWARI received the Ph.D. degree from Barkatullah University, Bhopal, India. He is currently a Teaching Fellow with the School of Electrical and Electronic Engineering, Newcastle University, U.K. He has background research in global navigation satellite system, channel modeling, wireless location, and GNSS software receiver designing and remote sensing. His research interests include space weather effect on GPS. He participated as a Scientist at XXVI Indian Scientific Expedition to Antarctica.

In Antarctica, he studied the effect of Aurora on GPS receiver and also did several experiments in marine navigation using GPS receiver, the results published in a book chapter title *Antarctica: The Most Interactive Ice-Air-Ocean Environment*. He has authored 15 journal papers, and PI of EPSRC IAA KTS project. He received various prestigious awards, including the Young Scienctist Award from Indian Science Congress, Bhopal Chapter, India, and the Young Scientist Award in 2011 from the International Union of Radio Science.

ALI H. MUQAIBEL (M'03–SM'12) received the B.Sc. and M.Sc. degrees from the King Fahd University of Petroleum and Minerals (KFUPM), Dhahran, Saudi Arabia, in 1996 and 1999, respectively, and the Ph.D. degree from the Virginia Polytechnic Institute and State University, Blacksburg, Virginia, in 2003. During his study at Virginia Tech, he was with both the Time Domain and RF Measurements Laboratory and the Mobile and Portable Radio Research Group. He is currently an Associate Professor with the Electrical Engineering Department, KFUPM.

He was a Visiting Associate Professor with the Center of Advanced Communications, Villanova University, Villanova, PA, USA, in 2013, and a Visiting Professor with the Georgia Institute of Technology in 2015. He has authored two book chapters and over 75 articles. His research interests include the direction of arrival estimation, through-wall-imaging, localization, channel characterization, and ultra-wideband signal processing. He received many awards in the Excellence in teaching, advising, and instructional technology.